JACS
JOURNAL OF THE AMERICAN CHEMICAL SOCIETY
pubs.acs.org/JACS
Article

Regulating Na-Ion Occupations of P-Type $Na_{0.67}Ti_{0.10}Fe_{0.05}Mn_{0.85}O_2$ for Improving Electrochemical Reversibility and Kinetics

Meijing Xiao,◆ Ce Zhou,◆ Wujie Dong,*,◆ Yuge Cao, Tianxun Cai, Shiyu Zhang, ZhengYao Li, Kai Sun, Dongfeng Chen, Hongliang Dong, Wei Zhao,* Hui Bi,* and Fuqiang Huang*

Cite This: J. Am. Chem. Soc. 2026, 148, 11228−11239
Read Online
ACCESS | Metrics & More | Article Recommendations | Supporting Information

ABSTRACT: P′2-type manganese-based layered oxides (Na_xMnO_2, $0.5 < x < 0.8$ usually) have emerged as promising cathode materials for sodium-ion batteries (SIBs), primarily due to their ability to deliver higher capacity compared to P2-type layered oxides. However, the underlying mechanism behind this high capacity still remains unclear, and the cycling stability has been a challenge. Given that distinct Na^+ occupation environments (edge-shared Na_e and face-shared Na_f) in P-type cathodes have different electrochemical kinetics, this study establishes a direct correlation between the high capacity of the P′2 structure and the high Na_e/Na_f ratio. The theoretical simulation confirms that the P′2 structure can accommodate more Na^+ at the Na_e site, which features a lower migration energy barrier and enhanced migration. Guided by this insight, a dual-approach rational design—combining quenching treatment and Ti/Fe codoping—is proposed to harvest the high-capacity and high-stability P′2-$Na_{0.67}Ti_{0.1}Fe_{0.05}Mn_{0.85}O_2$ cathode. Quenching enables the formation of P′2-structure with a high Na_e/Na_f ratio of 2.1 (compared to the typical ∼ 1.00), delivering a higher capacity of 190.3 mAh g^{-1} at 0.1 C between 2.0 and 4.0 V (the naturally cooled cathode only exhibits 130.2 mAh g^{-1} at 0.1 C); Furthermore, Ti^{4+} ($3d^0$, unfilled) and Fe^{3+} ($3d^5$, half-filled) are introduced into P′2-$Na_{0.67}MnO_2$ for suppressing Na^+/vacancy ordering and stabilizing the structure, resulting in excellent cycle stability with 96.9% capacity retention after 350 cycles at 5 C. This strategy provides a pathway to improve the reversible capacity of Mn-based layered cathodes for sodium-ion batteries.

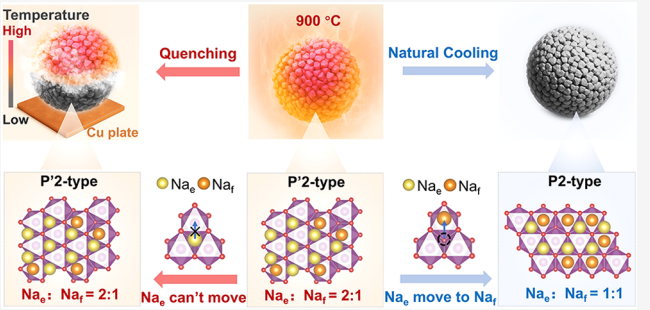

INTRODUCTION

Achieving high reversible capacity remains a central challenge in the development of advanced cathode materials for sodium-ion batteries (SIBs).[1−7] Among these, P-type manganese-based layered oxides (Na_xMnO_2, $0.5 < x < 0.8$ usually) have attracted considerable interest due to their high theoretical specific capacity, less phase transition and fast Na^+ kinetics.[8−10] Particularly, P′2-type layered oxides have emerged as promising cathodes, as they are capable of delivering significantly higher capacity compared to P2-type cathodes under similar operating conditions.[11−13] However, the mechanism of this increased capacity in P′2-type structures remains poorly understood, and the capacity fades rapidly due to the extensive Na^+ (de)intercalation, which often induces phase transitions, Na^+/vacancy ordering, and eventual structural collapse.[14,15]

The P2 phase adopts hexagonal symmetry ($P6_3/mmc$), whereas the P′2 phase is a distorted polymorph with orthorhombic symmetry ($Cmcm$).[16] The in-plane distortion is quantified by δ, defined through $b_{ortho}/a_{ortho} = (1 + \delta)\sqrt{3}$, where $\delta = 0$ corresponds to the ideal hexagonal P2 structure. When Jahn−Teller distortion (e.g., increased Mn^{3+}) induces b-axis elongation and/or a-axis shrinkage ($\delta > 0$), the orthorhombic P′2 phase becomes a more appropriate structural description.[25,26] This structural distortion is expected to influence Na^+ migration behavior, which is considered to play a key role in the unique electrochemical behavior and enhanced capacity.

P-type layered oxides have two distinct Na^+ sites: Na_e (edge-sharing sites at (1/3,2/3,3/4) coordinated with six TMO_6 octahedra by [Na_eO_6] prisms) and Na_f (face-sharing sites at (0,0,1/4) coordinated with two TMO_6 octahedra by [Na_fO_6] prisms).[22] Na_e exhibits a lower barrier energy, enabling faster Na^+ diffusion, whereas Na_f exhibits a high electrostatic repulsion (with a Na^+−Mn^{n+} distance of only 2.8−3.0 Å), leading to increased stress, a higher diffusion barrier, and Na^+/vacancy ordering structure during Na^+ (de) intercalation.[22,27] Therefore, increasing the Na_e/Na_f ratio directly enhances Na^+ mobility by occupying more Na_e sites with low barrier energy

Received: December 30, 2025
Revised: February 25, 2026
Accepted: February 27, 2026
Published: March 5, 2026

Table 1. Electrochemical Property Comparison of P-Type Na Layered Oxide Cathodes with Different Na_e/Na_f Ratios[a]

sample	Na_e/Na_f	voltage range (V)	capacity/current density	capacity retention	refs
P2−$Na_{0.67}MnO_2$	**1.15**	1.5−4.4	198 mAh·g^{-1}/10 mA·g^{-1}	87% (10 mA·g^{-1}, 20 cycles)	16
P2−$Na_{0.67}Fe_{0.5}Mn_{0.5}O_2$	**1.39**	1.5−4.0	161 mAh·g^{-1}/15 mA·g^{-1}	64% (150 mA·g^{-1}, 100 cycles)	17
P2−$Na_{0.67}Ni_{0.15}Mn_{0.85}O_2$	**1.00**	2.0−4.35	141 mAh·g^{-1}/20 mA·g^{-1}	96% (100 mA·g^{-1}, 120 cycles)	18
P2−$Na_{0.75}Ca_{0.04}Li_{0.1}Ni_{0.2}Mn_{0.67}O_2$	**1.56**	2.0−4.3	133 mAh·g^{-1}/10.7 mA·g^{-1}	95% (535 mA·g^{-1}, 200 cycles)	19
P2−$Na_{2/3}Mn_{0.72}Cu_{0.22}Mg_{0.06}O_2$	**1.49**	2.0−4.5	108 mAh·g^{-1}/17.4 mA·g^{-1}	88% (174 mA·g^{-1}, 100 cycles)	20
P2−$Na_{0.75}Ca_{0.05}Li_{0.15}Fe_{0.2}Mn_{0.6}O_2$	**1.85**	1.5−4.3	183 mAh·g^{-1}/22 mA·g^{-1}	76% (220 mA·g^{-1}, 150 cycles)	21
P2−$Na_{0.696}Ni_{0.329}Mn_{0.671}O_2$	**1.69**	2.0−4.13	88 mAh·g^{-1}/85 mA·g^{-1}	72% (170 mA·g^{-1}, 1000 cycles)	22
P2−$Na_{0.67}Ni_{0.21}Li_{0.05}Zn_{0.07}Mn_{0.67}O_2$	**1.57**	2.0−4.5	153 mAh·g^{-1}/12 mA·g^{-1}	81% (600 mA·g^{-1}, 200 cycles)	23
P2−$Na_{0.67}Ni_{0.28}Zn_{0.05}Mn_{0.62}Ti_{0.05}O_2$	**1.70**	2.0−4.3	120 mAh·g^{-1}/15 mA·g^{-1}	92% (150 mA·g^{-1}, 100 cycles)	24
P′2-$Na_{0.64}MnO_2$	**2.5**	1.5−4.4	216 mAh·g^{-1}/10 mA·g^{-1}	94% (10 mA·g^{-1}, 25 cycles)	16
P′2-$Na_{0.67}Fe_{0.1}Mn_{0.9}O_2$	**2.14**	2.0−4.0	171 mAh·g^{-1}/100 mA·g^{-1}	82% (100 mA·g^{-1}, 50 cycles)	25
P′2-$Na_{0.67}Ti_{0.1}Fe_{0.05}Mn_{0.85}O_2$	**2.1**	**2.0−4.0**	**190 mAh·g^{-1}/20 mA·g^{-1}**	**97% (1000 mA·g^{-1}, 350 cycles)**	**rhis work**

[a]Data were compiled from literature employing consistent Na-site crystallographic definitions and comparable refinement.

and has a higher capacity in the same voltage range, which is an important means of improving electrochemical performance in layered oxide cathodes.

Recent studies on the Na^+ sites modulation and its influence on the electrochemical behavior of P2-type layered cathodes are in progress. For example, controlling the Na content effectively regulates Na^+ occupation at different sites: $Na_{0.696}Ni_{0.329}Mn_{0.671}O_2$ (Na_e/Na_f = 1.69) exhibits superior electrochemical properties to $Na_{0.671}Ni_{0.333}Mn_{0.667}O_2$ (Na_e/Na_f = 1.64) and $Na_{0.745}Ni_{0.326}Mn_{0.674}O_2$ (Na_e/Na_f = 1.68).[22] Meanwhile, elemental doping offers another route to increase the ratio of Na_e/Na_f. Sb^{5+} substituted P2−$Na_{0.67}Mn_{0.61}Ni_{0.28}Sb_{0.11}O_2$ exhibits a high Na_e/Na_f ratio, attributed to the strong electrostatic repulsion between Sb^{5+} and Na_f, which drives Na^+ transport toward Na_e site. This redistribution enhances Na^+ mobility due to the lower migration barrier at Na_e site.[27] Similarly, Nb^{5+} substitution can also increase the Na_e/Na_f ratio, resulting in better rate performance and low-temperature cycling performance.[28] Dual-element substitution, such as Li/Zn cosubstitution, can lead to a larger energy difference between Na_e and Na_f sites, which facilitates the preferential occupation of Na^+ at Na_e sites with lower energy, making Na^+ easier to migrate.[23] In summary, the excellent electrochemical performance of the P2 structure is closely related to the high Na_e/Na_f ratio.

Inspired by the above materials, it was found that P′2-type layered oxides have a higher Na_e/Na_f ratio compared to P2, corresponding to the higher capacity (Table 1). Usually, P′2-type samples possess a Na_e/Na_f ratio around 2.0 and deliver capacity close to 200 mAh·g^{-1}, while P2-type samples show a lower Na_e/Na_f ratio of approximately 1.5, with corresponding capacity of ∼150 mAh·g^{-1}. Notably, P′2-$Na_{0.64}MnO_2$ with a high Na_e/Na_f ratio of 2.5 exhibits an ultrahigh capacity of 216 mAh·g^{-1}. However, the cycling stability remains limited owing to the Jahn−Teller effect of Mn^{3+}.

Hence, we design a Ti/Fe codoping P′2-$Na_{0.67}Ti_{0.1}Fe_{0.05}Mn_{0.85}O_2$ cathode with a high Na_e/Na_f ratio of 2.1 through quenching treatment. It is demonstrated that quenching can acquire P′2 structure with a high Na_e/Na_f ratio. Meanwhile, appropriate Ti/Fe cosubstitution could stabilize the $Na_{0.67}MnO_2$ structure. Compared to the naturally cooled one, the quenched P′2-$Na_{0.67}Ti_{0.1}Fe_{0.05}Mn_{0.85}O_2$ delivers a superior specific capacity of 190.3 mAh·g^{-1} between 2.0−4.0 V, better rate performance of 120.0 mAh·g^{-1} at 2 C, as well as good cycling stability with 96.9% capacity retention after 350 cycles at 5 C. These performances are all superior to the naturally cooled one. This work successfully deciphers the Na sites modulation mechanism (Na_e/Na_f ratio) underlying the high capacity of the P′2 structure. It is found that theoretical calculations have verified the P′2 phase to accommodate more Na^+ at Na_e site and possess a higher Na_e/Na_f ratio, thereby enabling more efficient Na^+ diffusion and improved capacity, manifesting bright application prospects.

RESULTS AND DISCUSSION

Structure and Morphology

To better understand the P-type layered structure, the simple P′2-$Na_{0.67}MnO_2$ model was constructed and investigated. It can be found that there are two distinct Na sites in the structure, namely, Na_e and Na_f, both occupying trigonal prismatic sites between adjacent TMO_6 slabs (Figure 1a). [Na_eO_6] prism shares edges with six adjacent TMO_6 octahedra, and [Na_fO_6] prism shares faces with two TMO_6 octahedra (Figure 1b). As evidenced by the theoretical calculations[22] and experimental results, the migration barrier energy of Na_f is higher than that of Na_e, indicating that Na_e migrates more easily in the structure. This finding accounts for the higher capacity and better rate capability observed in materials with a high Na_e/Na_f ratio (Figure 1c). Guided by the above results, P′2-$Na_{0.67}Ti_xFe_{0.15-x}Mn_{0.85}O_2$ and P2-$Na_{0.67}Ti_xFe_{0.15-x}Mn_{0.85}O_2$ (x = 0.15, 0.10, and 0.05) were synthesized via a solid-state reaction. The fundamental difference between them is that the P′2 phase was obtained by quenching (QU), whereas the P2 phase was synthesized by natural cooling (NC). Among these, the quenched P′2-$Na_{0.67}Ti_{0.1}Fe_{0.05}Mn_{0.85}O_2$ has the best electrochemical properties in terms of cycling performance and capacity (Figure S1). Therefore, the following research focused on $Na_{0.67}Ti_{0.1}Fe_{0.05}Mn_{0.85}O_2$ (NTFM) materials.

Figure S2 illustrates a schematic of the synthesis process of the NTFM. The first image shows particles rapidly quenched from 900 °C onto a Cu plate, the second depicts the high-temperature (900 °C) synthesis state, and the third shows the material after natural cooling. The differently colored particles represent temperature changes through these steps. XRD patterns were collected at different temperatures to track the structural evolution of the material during the cooling process (Figure S3). Since the P phase is the dominant phase, the following discussion will focus on the differences and effects of the dominant phase. At 900 °C, the XRD patterns of NTFM matched well with the P′2 phase. As the temperature

https://doi.org/10.1021/jacs.5c23314
J. Am. Chem. Soc. 2026, 148, 11228−11239

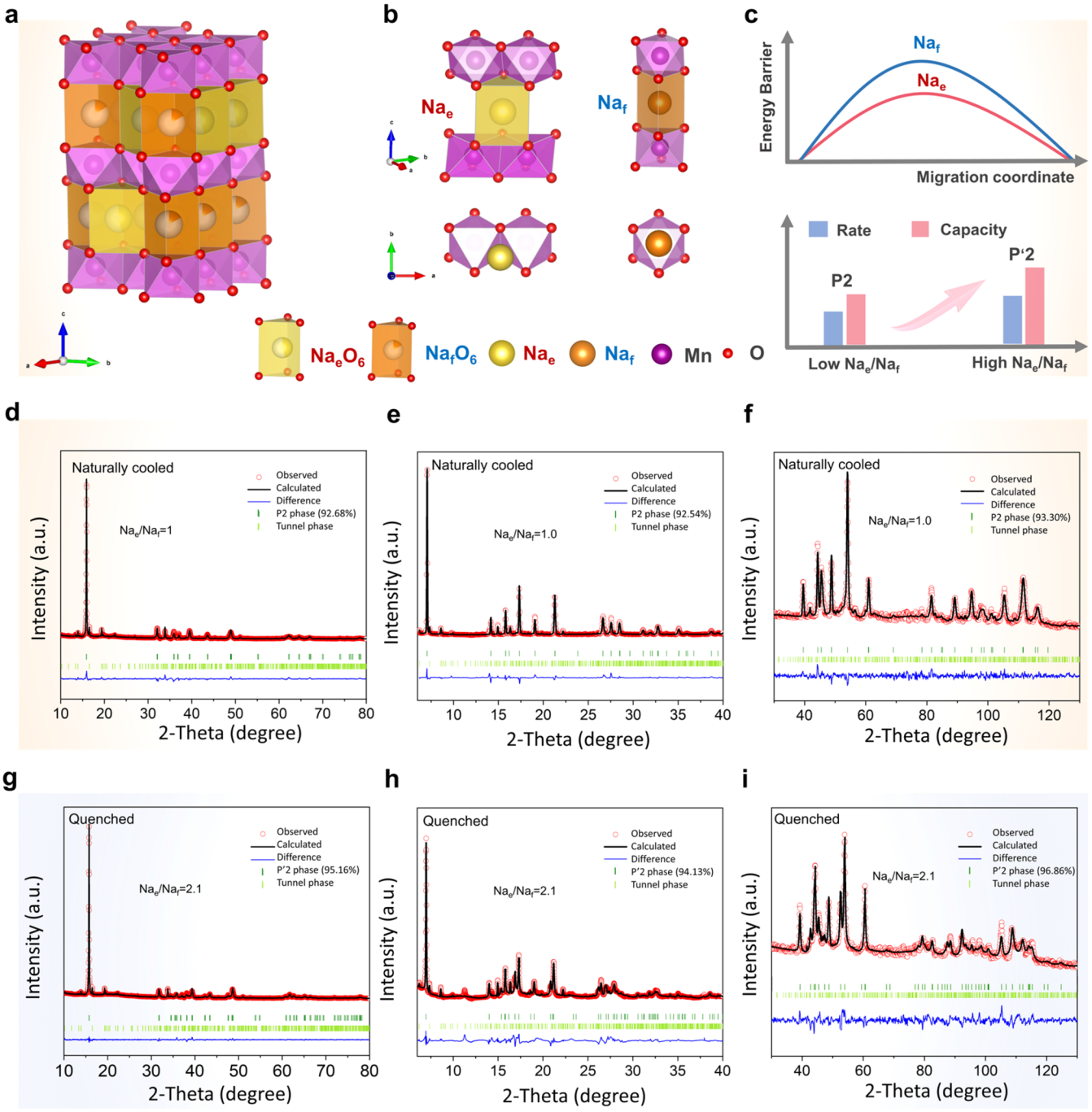

Figure 1. Structure and morphology. (a) Schematic crystal structures of P′2-$Na_{0.67}MnO_2$ at different views. (b) Structure schematic of Na_e and Na_f at different views (c) schematic graph of the migration energy barrier and the electrochemical properties. Rietveld refinement PXRD, SXRD, and NPD of (d−f) NTFM-NC and (g−i) NTFM-QU, respectively.

decreased, the signal corresponding to the P′2 phase gradually weakened, and the NTFM completely transformed into the P2 phase at 600 °C. This phenomenon is likely driven by the absorption of oxygen during cooling, which increases the Mn average valence and decreases the concentration of Mn^{3+} with the Jahn−Teller effect.[29] The XRD data at different temperatures clearly reveal that the structure of NTFM can be tailored by controlling the cooling rate. Rapid cooling facilitates the retention of the high-temperature phase (P′2 phase). To better fit the structure of NTFM, six structural models were constructed to match the quenched P′2-$Na_{0.67}Ti_{0.1}Fe_{0.05}Mn_{0.85}O_2$ (NTFM-QU) structure, and four structural models were constructed for the naturally cooled P′2-$Na_{0.67}Ti_{0.1}Fe_{0.05}Mn_{0.85}O_2$ (NTFM-NC) (Figures 1d,1g and S4). The results show that the model with the space group of *Cmcm* and the Na_e/Na_f ratio of 2.1 provides the best overall refinement quality for NTFM-QU among all candidates, and the model with a 1.0 Na_e/Na_f ratio and the $P6_3/mmc$ space group exhibits the best fitting results for NTFM-NC (Table S1). Importantly, Synchrotron X-ray diffraction (SXRD) was also performed to obtain higher-quality data (Figure 1e,h). The results obtained from refinement are consistent with PXRD (Figure S5 and Table S2), further confirming the difference in Na ratios in P2 and P′2 structures. ^{23}Na solid-

https://doi.org/10.1021/jacs.5c23314
J. Am. Chem. Soc. 2026, 148, 11228−11239

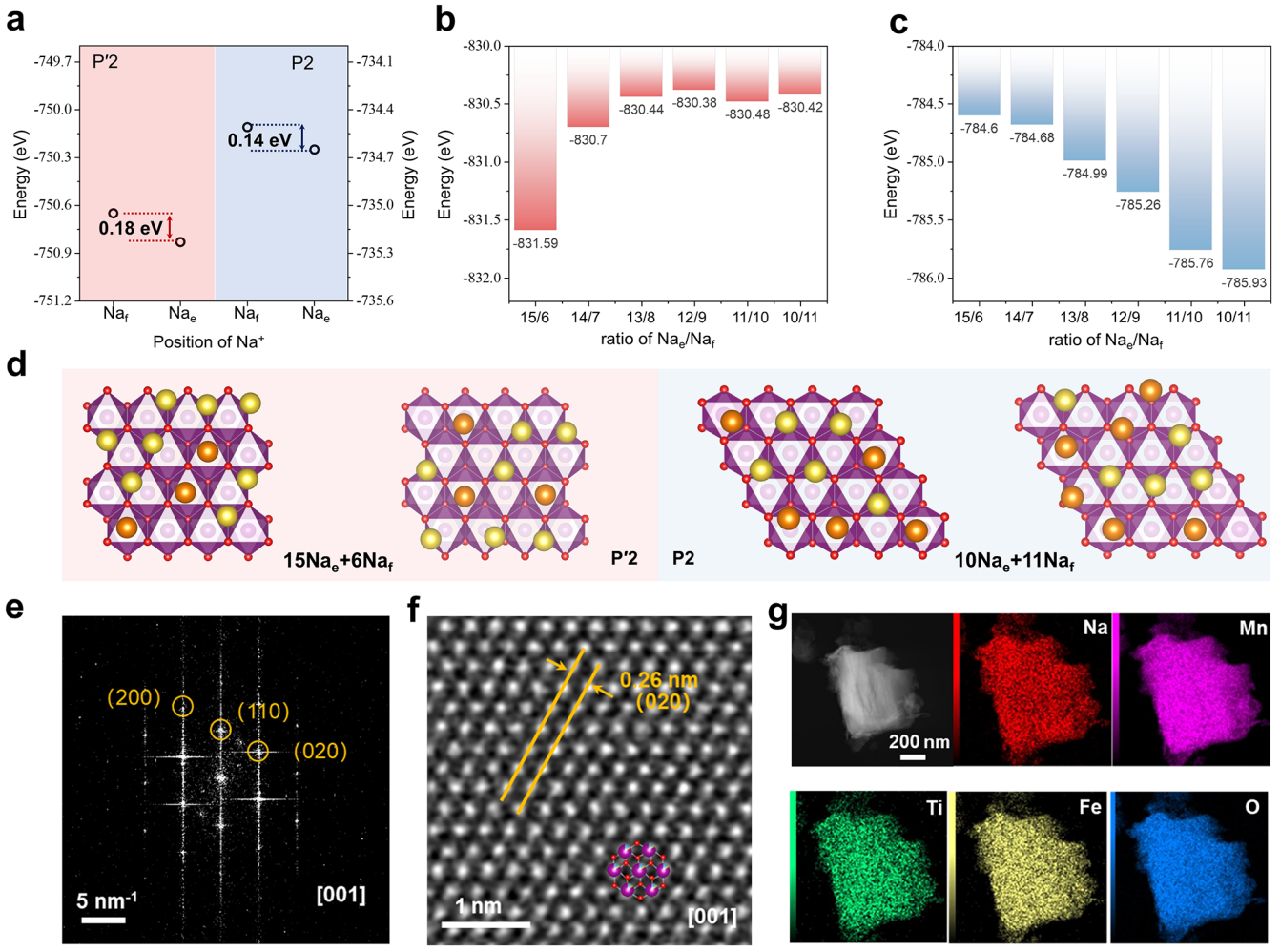

Figure 2. Structure and morphology. (a) Calculated energy difference between the Na_e and Na_f sites for NTFM-QU (red background) and NTFM-NC (blue background). The calculated system energy of (b) NTFM-QU and (c) NTFM-NC when Na^+ is filled into different sites. (d) Crystal structure calculated by the First-principles (e) SAED pattern. (f) HAADF-STEM images of NTFM-QU. (g) EDS mapping images of the NTFM-QU sample.

state nuclear magnetic resonance experiments can directly probe the local environment of Na.[30,31] It is demonstrated that the NTFM-QU exhibits a larger chemical shift than NTFM-NC (1240 ppm vs 1186 ppm), indicating a larger contribution from Na^+ occupying the Na_e sites of NTFM-QU, consistent with refinement results (Figure S6).[32,33] The NPD refinements enable reliable determination of Na occupancies and atomic displacement parameters, revealing an obvious difference in the Na_e/Na_f ratio between the two materials (Figure 1f,i). These results provide definitive, quantitative confirmation of the distinct Na-site distributions in the P2 and P′2 structures. Consequently, quenching emerges as an effective strategy to increase the Na_e/Na_f ratio, thereby enhancing Na^+ diffusion kinetics. The refined crystallographic parameters of NTFM-QU and NTFM-NC are summarized in Tables S3−S8.

In order to demonstrate the accuracy of the refined XRD experimental results regarding the Na_e/Na_f ratio, first-principal density functional theory (DFT) was adopted to analyze the preferred occupancy of Na_e and Na_f in both P2 and P′2-structures. The calculated total energy of Na_e and Na_f in both phases (Figure 2a) reveals that the energy of the Na_e site is lower than that of the Na_f site in both materials, which means Na^+ preferentially occupies the Na_e site. Furthermore, the system energy of the P′2 and P2-structures with different Na_e/Na_f ratios was calculated by constructing 12 possible crystal structures to examine how the Na^+ distribution affects the system energy (Figure S7). As shown in Figure 2b,c, the Na_e/Na_f ratio of the minimum system energy is 15/6 (2.5) for P′2 and 10/11 (0.91) for P2 (Figure 2d), demonstrating that more Na^+ will occupy the Na_e site in the P′2 structure, which is more favorable for the migration of Na^+, thus increasing the specific capacity. This result is in good agreement with the experimental data, and the minor discrepancy likely arises from the subtle effects of Ti/Fe codoping on local atomic configurations. Overall, this result highlights the correlation between the P′2 structure and the Na_e/Na_f ratio, emphasizing the importance of increasing the Na_e/Na_f ratio to improve the specific capacity of the materials.

The morphologies of NTFM-QU and NTFM-NC samples were further revealed by TEM. As shown in Figure S8, both samples display a block shape. Further HRTEM images (Figure S9) demonstrate that the average interplanar spacing of the (002) plane in NTFM-QU is 0.564 nm, which is larger than that of NTFM-NC (0.557 nm), consistent with the XRD refinement analysis results. The SEM image (Figure S10) shows that most particles of NTFM-QU are platelike particles,

https://doi.org/10.1021/jacs.5c23314
J. Am. Chem. Soc. 2026, 148, 11228−11239

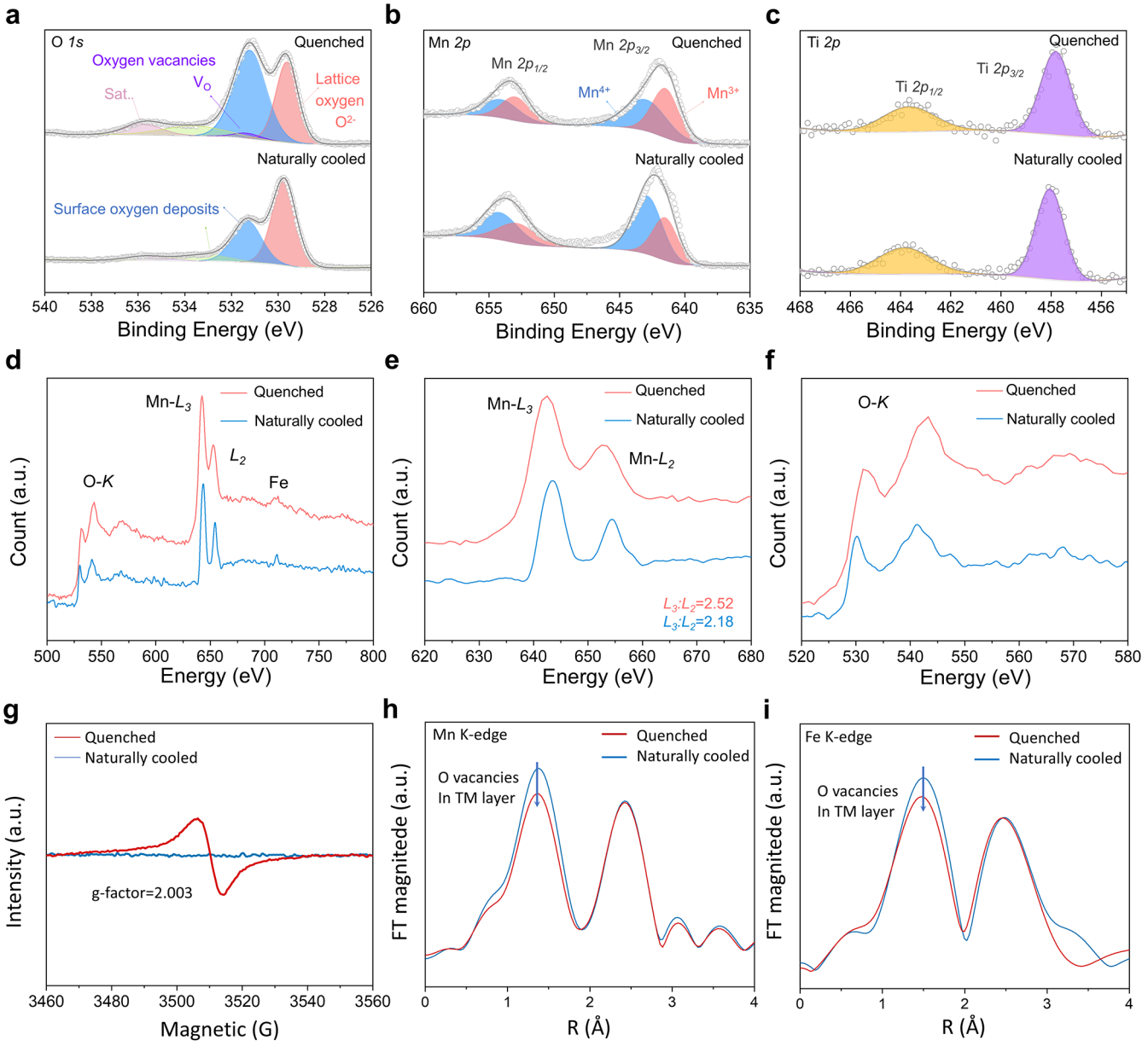

Figure 3. Characterizations of NTFM cathode materials. XPS spectra of NTFM-QU and NTFM-NC samples: (a) O 1s, (b) Mn 2p, and (c) Ti 2p. (d) Electron energy-loss spectra (EELS) of NTFM-QU and NTFM-NC. (e) EELS spectra of the Mn L-edge. (f) EELS spectra of the O K-edge. (g) EPR spectra of NTFM-QU and NTFM-NC. (h) Mn Fourier-transformed EXAFS spectra of NTFM-QU and NTFM-NC. (i) Fe Fourier-transformed EXAFS spectra of NTFM-QU and NTFM-NC.

and very few appear rod-shaped. In addition, the selected area electron diffraction (SAED) pattern of NTFM-QU (Figure 2e) further reflects the bright diffraction spots along the [001] axis, which is consistent with the HAADF-STEM imaging results and confirms the highly crystallized orthorhombic structure (Figures 2f and S11). Inductively coupled plasma optical emission spectrometry (ICP-OES, Table S9) demonstrates that the molar ratio conforms well with the anticipated value, and EDS mapping (Figures 2g and S12) reveals a uniform distribution of Na, Mn, Ti, Fe, and O elements in both NTFM-QU and NTFM-NC cathodes,[34] indicating successful and homogeneous doping.

Materials Characterization

The charge compensation mechanism of the NTFM cathode was systematically unveiled via XPS (Figure S13) analyses. As shown in the O 1s XPS spectra of NTFM (Figure 3a), peaks at 529.4 and 531.2 eV were observed in NTFM-QU, corresponding to lattice oxygen (O^{2-}) and oxygen vacancies (V_O), respectively. In contrast, no V_O was detected in NTFM-NC,[35−37] indicating that some Mn^{4+} in NTFM-QU tends to be reduced to Mn^{3+} with Jahn−Teller distortion for charge balance, and the proportion of Mn^{3+} in NTFM-QU is relatively higher than that in NTFM-NC. The presence of a large amount of Jahn−Teller active Mn^{3+} is the main contributor to capacity.[10] The Mn 2p spectra (Figure 3b) exhibit two pairs of peaks at 641.5, 653.1, 643.2, and 654.3 eV, corresponding to the Mn^{3+} $2p_{3/2}$, Mn^{3+} $2p_{1/2}$, Mn^{4+} $2p_{3/2}$, and Mn^{4+} $2p_{1/2}$, respectively.[38,39] In Figure 3c, the Ti 2p peaks of Ti^{4+} are observed at 457.8 and 463.7 eV, belonging to the Ti $2p_{3/2}$ and Ti $2p_{1/2}$ orbitals.[40] It is known that Ti^{4+} is electrochemically

https://doi.org/10.1021/jacs.5c23314
J. Am. Chem. Soc. 2026, 148, 11228−11239

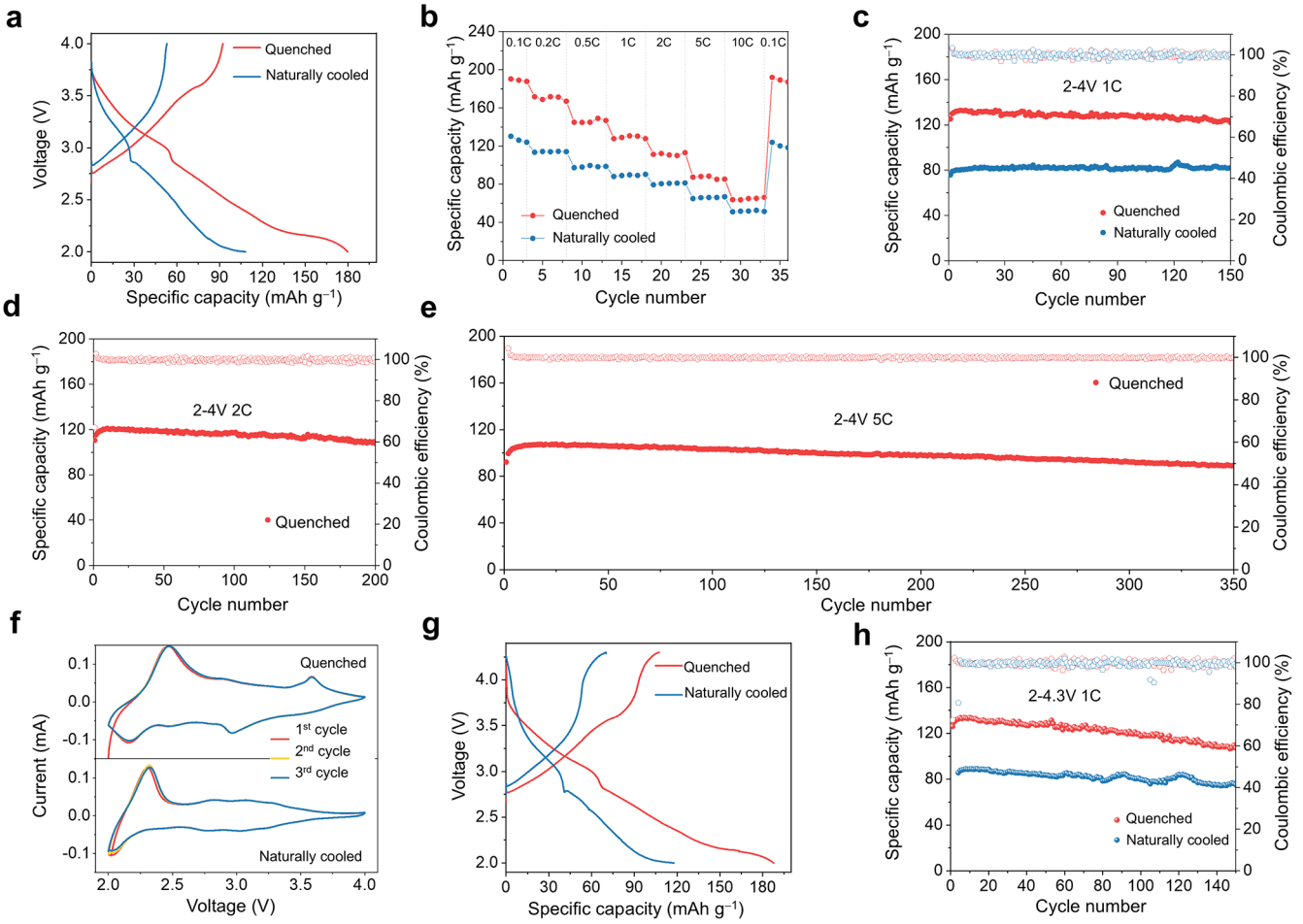

Figure 4. Electrochemical performance. (a) The charge and discharge curves during the first cycle for NTFM-QU and NTFM-NC samples between 2.0−4.0 V. (b) The rate performance of NTFM-QU and NTFM-NC samples at the rate of 0.1−10 C. (c) The cycle performance of NTFM-QU and NTFM-NC samples at 1 C between 2.0−4.0 V for 150 cycles. (d) The cycle performance at 2 C for 200 cycles. (e) The cycle performance at 5 C between for 350 cycles. (f) The CV curves of NTFM-QU and NTFM-NC samples at 0.1 mV s^{-1} in the first three cycles. (g) The charge and discharge curves during the first cycle for NTFM-QU and NTFM-NC samples between 2.0−4.3 V. (h) The cycle performance at 1C for 100 cycles.

inert in the cathode material and does not participate in redox reactions.

To probe the bulk information about charge compensation at the atomic scale, a focused ion beam (FIB) was employed, combined with scanning transmission electron microscopy (STEM) and electron energy loss spectroscopy (EELS). As illustrated in Figure S14, the layered structures of transition metals (TMs) in NTFM-QU and NTFM-NC along the [001] axis are clearly visible, where the bright dots correspond to TM ions. The EELS spectra of NTFM-QU and NTFM-NC are displayed in Figure 3d. The fine structure and chemical shift of the Mn L-edges (Figure 3e) and O K-edges (Figure 3f) provide deep insight into changes of electronic structure, as these edges are sensitive to their oxidation states.[41] Compared to NTFM-NC, the Mn L-edge of NTFM-QU shows a slight shift to lower energy, indicating a reduction of the average Mn oxidation state. In addition, a higher L_3/L_2 ratio (2.52) of NTFM-QU further proves that the oxidation state of Mn is reduced.[42] For the O *K*-edge prepeak, the intensity and position are also attributed to the oxidation state of O. It is clear that the prepeak/main-peak intensity of NTFM-QU is lower than that of NTFM-NC, indicating the existence of bulk V_O and the reduction of the holes in the 2p−3d hybrid orbital,[36,42] verifying the improved Mn redox activity after the introduction of oxygen vacancies. The slight right shift of this peak of NTFM-QU suggests that the O is in a higher valence state, which further means that the existence of V_O leads to an increase in the overall O oxidation state.[43−45] Moreover, measurements performed on different regions yielded consistent results, confirming the uniformity of these features throughout the material (Figure S15).

To further corroborate the existence of bulk V_O, electron paramagnetic resonance (EPR), a highly sensitive technology for detecting unpaired electrons, was employed.[45] It serves as an effective way for characterizing bulk V_O. As shown in Figure 3g, a clear signal at g = 2.003 in NTFM-QU is observed, which can be attributed to unpaired electrons associated with V_O.[32] Besides, the bulk Vo can alter the electronic and local structures of materials.[36] As shown in Figure S16, the Mn K-edge in NTFM-QU shifts to lower energy compared with NTFM-NC, indicating a reduced Mn oxidation state due to charge compensation from oxygen vacancies.[46] R-space spectra further reveal a decreased Mn−O shell intensity (Figure 3h), suggesting the lower average O coordination numbers.[47] Meanwhile, the Fe K-edge energy shows minimal change between the two materials (Figure S17), indicating that Fe

https://doi.org/10.1021/jacs.5c23314
J. Am. Chem. Soc. 2026, 148, 11228−11239

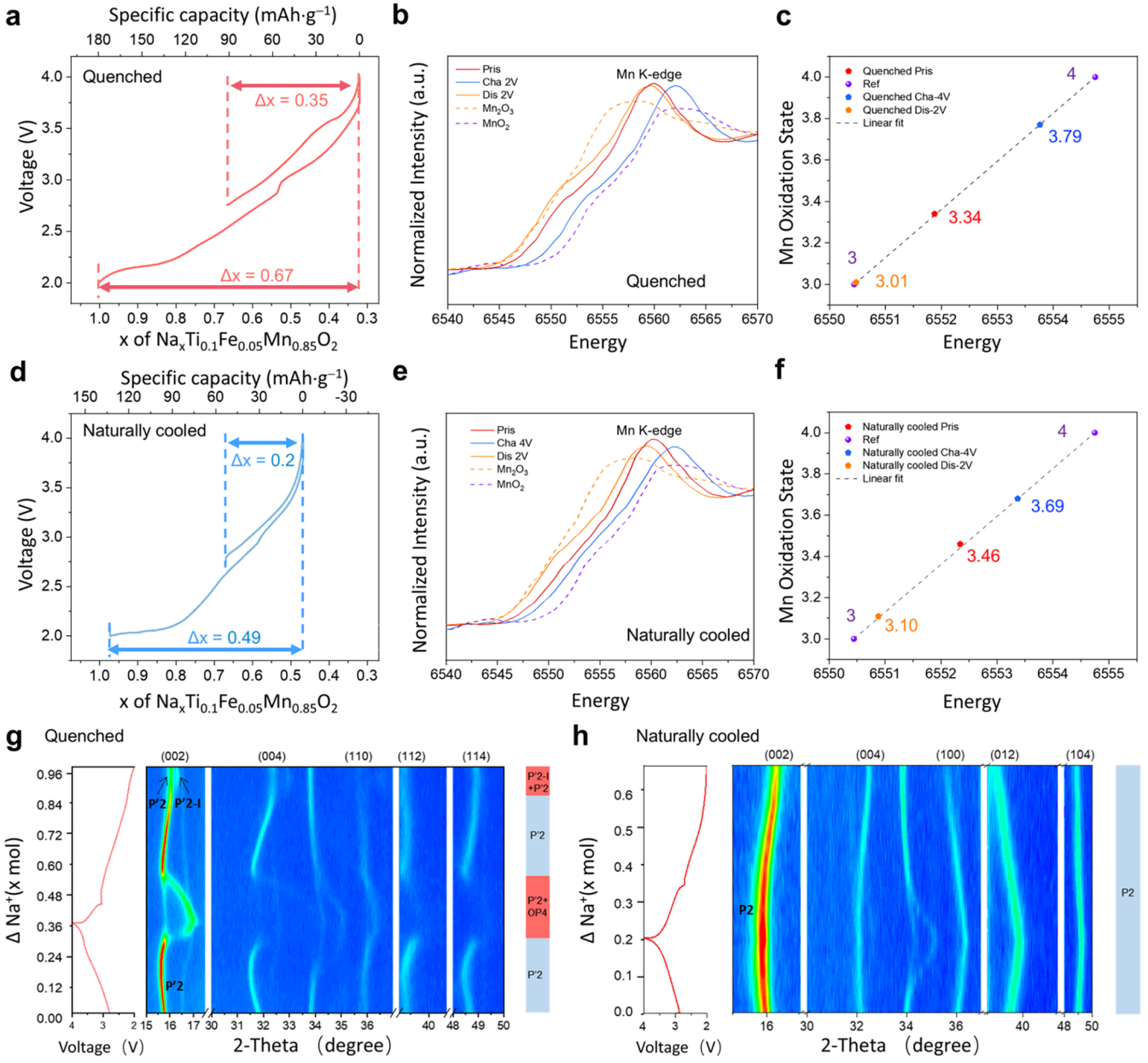

Figure 5. Charge compensation mechanism and structural evolution. The charge and discharge curves during the first cycle for (a) NTFM-QU and (d) NTFM-NC. Normalized Mn K-edge XANES spectra at different charge/discharge states for (b) NTFM-QU and (e) NTFM-NC. (c) and (f) Mn valence evolution determined by the integration method with the MnO2 and Mn_2O_3. Intensity contour maps of in situ XRD patterns during the first charge/discharge cycle of (g) NTFM-QU and (h) NTFM-NC samples.

does not participate in charge compensation. And the weakened Fe−O shell intensity in NTFM-QU further corroborates the presence of V_O (Figure 3i). Consistent with these results, EDS line-scan analyses reveal a reduced O/Mn count ratio in NTFM-QU (Figure S18), providing additional, independent evidence for V_O.[36,45,48]

Electrochemical Performance

The electrochemical measurements of NTFM were carried out in Na half-cells. Figure 4a shows the galvanostatic charge/discharge curves of NTFM-QU and NTFM-NC at 0.1 C during the first cycle. NTFM-QU exhibits two voltage plateaus at ∼2.2 V and ∼3.5 V, suggesting a phase transition to the P′2-I and OP4 phase. In addition, the capacity of NTFM-QU is higher than that of NTFM-NC, which is attributed to the higher Na_e/Na_f ratio of NTFM-QU, and thus, more Na^+ locating at Na_e site can migrate easily. As shown in Figures 4b and S19, NTFM-NC delivers a reversible capacity of 130.2−52.6 mAh·g^{-1} at 0.1−10 C. In contrast, the capacity of NTFM-QU increases to 190.3−66.3 mAh·g^{-1} over the same range, illustrating that NTFM-QU has better rate capability than NTFM-NC. Besides, NTFM-QU delivers a capacity of 130.6 mAh·g^{-1} at 1C (Figure 4c), which is over 40 mAh·g^{-1} higher than that of NTFM-NC. Figure 4d,e present the excellent cycling performance of the NTFM-QU at 2 and 5 C, respectively. It delivers a discharge capacity of 109.1 mAh·g^{-1} after 200 cycles at 2 C, with the capacity retention of approximately 90.3%. Even at a high rate of 5 C, NTFM-QU retains about 96.9% of the initial capacity after 350 cycles, with an average Coulombic efficiency of 99.6% (excluding the first cycle).

https://doi.org/10.1021/jacs.5c23314
J. Am. Chem. Soc. 2026, 148, 11228−11239

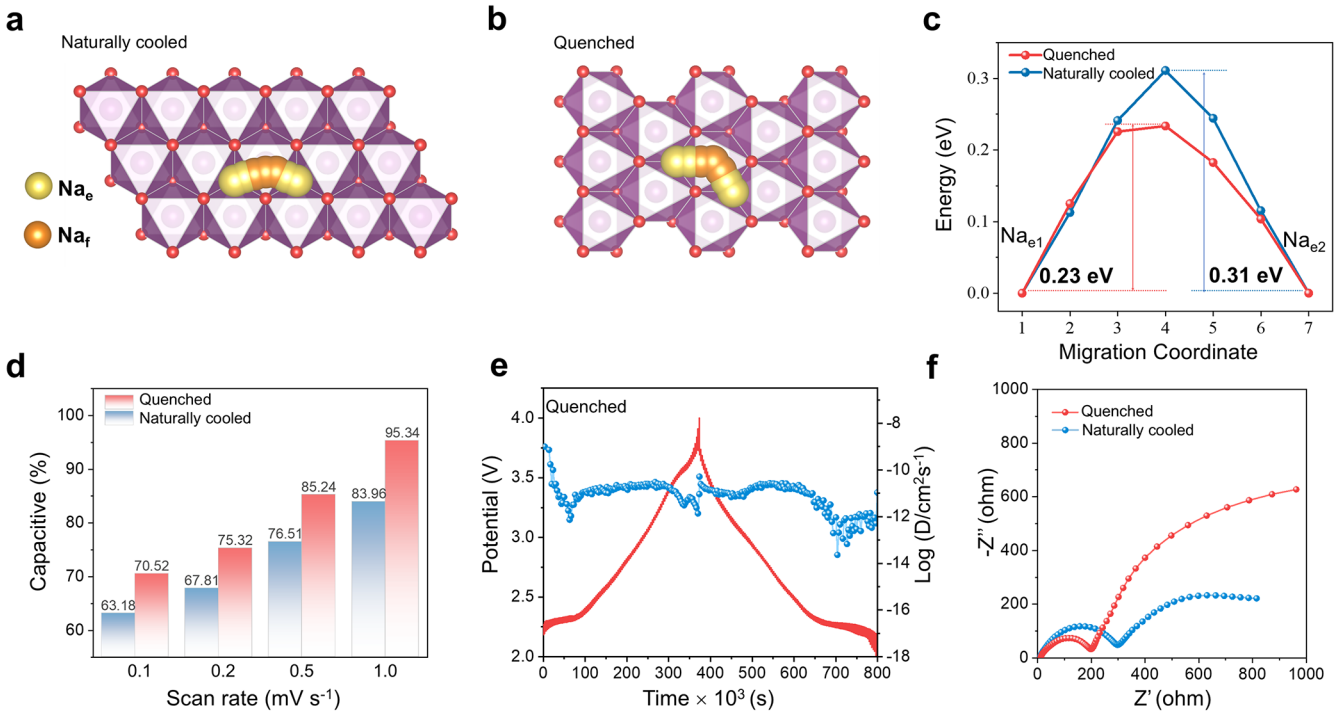

Figure 6. Na^+ kinetic analyses. Crystal structure viewed along the *c* axis for Na^+ migration paths between two adjacent equivalent Na_e sites in (a) NTFM-QU and (b) NTFM-NC. (c) Na^+ migration energy barriers. (d) Capacitive contributions at different scan rates. (e) Charge−discharge GITT profiles of NTFM-QU in the second cycle at 20 mA·g^{-1} and the corresponding Na^+ diffusion coefficients (D_{Na^+}). (f) Nyquist plots of NTFM-QU and NTFM-NC.

The initial three CV curves of NTFM-QU and NTFM-NC between 2.0 and 4.0 V at a scan rate of 0.1 mV·s^{-1} are illustrated in Figure 4f. Multiple pairs of redox peaks are observed in both samples, corresponding to the multiple voltage plateaus in the charge/discharge profiles (Figure 4a). For both samples, the redox pairs near 2.60/2.80 V are associated with Na^+/vacancy ordering. In addition, the redox peaks at 2.46/2.17 V for NTFM-QU and 2.30/2.00 V for NTFM-NC are assigned to the Mn^{3+}/Mn^{4+} redox couple and are often accompanied by the structural phase transitions. Notably, the redox voltage of NTFM-QU is higher than that of NTFM-NC, which can be attributed to a higher degree of structural distortion in the original P′2 phase.[49] The extra redox peaks of NTFM-QU above 3 V are associated with the appearance of the OP4 phase.

To further investigate the impact of quenching on the high-voltage performance of NTFM, the cutoff voltage was increased to 4.3 V. NTFM-QU and NTFM-NC both show an additional charging plateau of about 4.2 V in the initial charge curve (Figure 4g), which corresponds to O oxidation and normally leads to harmful O_2 release. Thus, the cycling stability of both materials decreases as depicted in Figure 4h. Nevertheless, NTFM-QU maintains a higher capacity than NTFM-NC throughout the cycling test, highlighting the positive impact of quenching on Na^+ transport. All the above results demonstrate that the NTFM-QU is a promising cathode material for sodium ion batteries.

Charge Compensation Mechanism and Structural Evolution

To further clarify the charge compensation mechanism of NTFM-QU and NTFM-NC, ex situ X-ray absorption near-edge structure (XANES) was employed to track the electronic structure changes during the first cycle (Figure 5a,d). Mn K-edge spectra of NTFM-QU (Figure 5b) and NTFM-NC (Figure 5e) at different charge/discharge states were collected, and the corresponding Mn oxidation states were quantified using an integration method[36] (Figure 5c,f and Note S1), as previously reported. The initial valences of Mn were calculated to be +3.34 for NTFM-QU and +3.46 for NTFM-NC, with the lower valence in NTFM-QU attributed to the formation of V_O induced by quenching. During the charging process, the Mn *K*-edge spectrum of NTFM-QU shows a more apparent shift toward high energy compared to NTFM-NC, consistent with the fact that the initial charge capacity of NTFM-QU (92.25 mAh·g^{-1}) is much higher than that of NTFM-NC (52.72 mAh·g^{-1}). After discharging to 2.0 V, the Mn valence of NTFM-QU decreases from +3.79 to +3.01, in contrast to the reduction from +3.69 to +3.10 for NTFM-NC. This redox behavior correlates well with the changes of Na^+ content observed in Figure 5a,d, indicating that only Mn ions contribute to the capacity during charge/discharge, and Fe is not redox active below 4 V. Ti and Fe serve to stabilize the structure during cycling. Consequently, the interaction between high manganese redox activity induced by V_O and high Na_e/Na_f ratio leads to the increased capacity of NTFM-QU, while Ti and Fe without redox activity play a role in stabilizing the structure.

In situ XRD measurement was performed at 2.0−4.0 V to investigate the structural phase evolution of NTFM-QU and NTFM-NC during Na^+ extraction and insertion (Figures 5g,h and S20). For NTFM-QU, upon the Na^+ extraction, the (002) and (004) peaks gradually shift to a lower degree, indicating an expansion of interlayer spacing and *c*-parameter caused by increased electrostatic repulsion between adjacent oxygen layers.[50] Meanwhile, the (110), (112), and (114) peaks shift to higher angles, suggesting the oxidation of Mn^{3+}, which results in the shrinkage of the ab plane. When charging to 3.5 V, the

https://doi.org/10.1021/jacs.5c23314
J. Am. Chem. Soc. 2026, 148, 11228−11239

(002) and (004) peaks weaken, and a new peak emerges at 17°, corresponding to the (004) plane of the OP4 phase. This phase results from interlayer sliding of the transition metal slabs and is considered an intermediate phase between the P2 and O2 structures. The P′2-OP4 phase transition has been reported to be more reversible than the conventional P′2-O2 transition.[51,52] Notably, the formation of the OP4 phase does not involve oxygen loss, as evidenced by the absence of any high-voltage plateau associated with oxygen redox and by the identical charge/discharge profiles before and after cycling (Figure S21), which collectively confirm the high reversibility of the P′2-OP4 transition.[53−55] During the following discharge process (Na^+ insertion), the OP4 phase gradually reverts to the P′2 phase owing to the Jahn−Teller distortion of Mn^{3+}. Meanwhile, the (002) peak shifts back to a higher degree, indicating a contraction of the interlayer spacing and a decrease in the *c*-parameter. At the same time, the in-plane reflections move to lower angles, suggesting the recovery of the ab lattice parameters as Mn is reduced. Figure S20b illustrates the change of phase fractions throughout the process, revealing that even charging to 4 V, the structure does not transform into the O2 phase, demonstrating high structural reversibility. When the discharge voltage is below 2.2 V, similar to the P′2 phase, a lattice-distorted P′2-I phase occurs due to the continued increase of Mn^{3+}. This low-voltage region is accompanied by a lattice distortion and further evolution of lattice parameters, reflecting enhanced Jahn−Teller effects associated with high Mn^{3+} content. The phase fractions are shown in Figure S20c. This observation confirms the Mn ions of NTFM-QU are reduced to lower valence, in agreement with the change of Mn valence in Figure 5c,f.

The phase transition behavior of NTFM-NC was also examined (Figures 5h and S20d). It is noted that no reflections corresponding to the OP4 or P′2 phases were observed during the charge/discharge process; only the P2-phase peaks exhibited continuous shifts, indicating that a solid-solution reaction predominates in this voltage range. The (002) and (004) peaks of P2 shift to a lower angle during charging and revert to a higher angle during discharging, consistent with an initial increase followed by a decrease in the c parameter. In contrast, the variation of the (100), (012), and (104) peaks was related to the Mn redox reaction, corresponding to the a/b parameter contracting during charging and expanding during discharging. This entire process signifies a reversible phase evolution of the material. The distinct phase transitions between NTFM-QU and NTFM-NC can be attributed to the differences in Na^+ occupation environments and the content of Na^+ (de)intercalation, which is responsible for the difference in electrochemical behaviors.

Na^+ Kinetic Analyses

To investigate the Na^+ diffusion kinetics of NTFM, the climbing image nudged elastic band (CI-NEB) method was carried out to calculate the Na^+ migration barrier (E_a). Since the energy of Na_e site is lower than Na_f site, the diffusion path of Na^+ was designed as Na_{e1}−Na_f−Na_{e2} for the two models, as clearly shown in Figure 6a,b. The calculated result displays that NTFM-QU exhibits a smaller E_a of 0.23 eV compared to 0.31 eV for NTFM-NC, demonstrating that Na^+ migrates more easily in NTFM-QU (Figure 6c).

Transport kinetics are a crucial indicator of electrochemical performance. To evaluate the contribution of capacitance, CV measurements were conducted at various scanning rates. The CV curves of NTFM-QU and NTFM-NC are shown in Figure S22, and the corresponding computational equations are presented in Note S2. The linear relationship of $\log(i)$ and $\log(v)$ for peaks 1, 2, and 3 is plotted in Figure S23. The obtained values of b for NTFM-QU are 0.68, 0.85, and 0.90, and for NTFM-NC are 0.52, 0.99, and 0.93, respectively. These values indicate that the electrochemical reactions of both samples are controlled by both capacitance and diffusion processes. The ratio of diffusion and capacitance control can be quantitatively analyzed by the equation

$$i = k_1 v + k_2 v^{0.5} \quad (1)$$

where i is the peak current, v represents the scanning rate, and $k_1 v$ and $k_2 v^{0.5}$ mean the capacitance and Na^+ diffusion, respectively. The values of k_1 and k_2 are gained by plotting $iv^{-0.5}/v^{0.5}$. Figure 6d shows the diffusion-controlled coefficient at different scan rates. The capacitive contribution of NTFM-QU ranges from 70.52% to 95.34%, whereas that of NTFM-NC varies between 63.18% and 83.96% over the same scan rate range. Such high capacitive-like capacity is even outstanding in supercapacitor materials,[56] which may be due to the loosely packed crystal structure.[57] Galvanostatic intermittent titration technique (GITT) and electrochemical impedance spectroscopy (EIS) were performed to characterize the bulk and surface/interface kinetics, respectively. As illustrated in Figures 6e and S24, the apparent diffusion coefficient D_{Na^+} (Figure S25) increases from 1.25×10^{-11} to 4.33×10^{-10} $cm^2 \cdot s^{-1}$ after quenching treatment, confirming that quenching treatment effectively enhances the interfacial transport performance of SIBs. Meanwhile, the charge-transfer resistance (R_{ct}) decreases from 359.8 to 195.9 Ω (Figure 6f), indicating a significant advantage of NTFM-QU in transfer kinetics. Both experimental and calculated results demonstrate that quenching treatment facilitates the diffusion of Na^+ and migration of e^-, ultimately leading to the improvement of electrochemical performances.

CONCLUSIONS

In summary, this work unravels the critical role of Na^+ site occupancy in determining the electrochemical performance of P-type manganese-based layered oxides and the correlation between the high Na_e/Na_f ratio and the high capacity of P′2-type cathodes, where P′2-type cathodes can accommodate more Na^+ at Na_e site, which possesses a lower barrier energy and easier (de)intercalation. Therefore, P′2-$Na_{0.67}Ti_{0.1}Fe_{0.05}Mn_{0.85}O_2$ cathode with a Na_e/Na_f ratio of 2.1 is synthesized through quenching treatment, which is regarded as an effective strategy to improve capacity (P′2-structure acquired by quenching) and stabilize the structure (Ti and Fe codoping). The specific capacity of the $Na_{0.67}Ti_{0.1}Fe_{0.05}Mn_{0.85}O_2$ sample is significantly improved to 190.3 $mAh \cdot g^{-1}$ (30% higher capacity than naturally cooled), owing to the increasing Nae site occupation in the quenched $Na_{0.67}Ti_{0.1}Fe_{0.05}Mn_{0.85}O_2$. Besides, the specific capacity remains up to 94.3 $mAh \cdot g^{-1}$ after 350 cycles with 96.9% capacity retention even at 5 C, indicating exceptional rate performance. This result demonstrates that regulating the Na_e/Na_f ratio through controlled synthesis and rational doping is an effective strategy to enhance the capacity and stability of Mn-based layered cathodes, which offers a pathway to optimize cathode materials.

https://doi.org/10.1021/jacs.5c23314
J. Am. Chem. Soc. 2026, 148, 11228−11239

■ ASSOCIATED CONTENT

Supporting Information

The Supporting Information is available free of charge at https://pubs.acs.org/doi/10.1021/jacs.5c23314.

Details of materials synthesis and characterizations, electrochemical measurements, and theoretical calculations; refine XRD, ss-NMR, TEM, HRTEM, SEM, HAADF-STEM, EDS, XPS, EELS, XANES, GITT, and ICP data; electrochemical results; lattice parameters of NTFM-QU and NTFM-NC; and fitted refine results of NTFM-QU and NTFM-NC (PDF)

■ AUTHOR INFORMATION

Corresponding Authors

Wujie Dong − *Key laboratory of Intelligent Creation for Extreme Energy Materials of the Ministry of Education, School of Materials Science and Engineering, and Zhang Jiang Institute for Advanced Study, Shanghai Jiao Tong University, Shanghai 200240, China;* orcid.org/0000-0003-4828-4439; Email: dongwujie@sjtu.edu.cn

Fuqiang Huang − *Key laboratory of Intelligent Creation for Extreme Energy Materials of the Ministry of Education, School of Materials Science and Engineering, and Zhang Jiang Institute for Advanced Study, Shanghai Jiao Tong University, Shanghai 200240, China; Inner Mongolia Research Institute, Shanghai Jiao Tong University, Hohhot 010010, China;* orcid.org/0000-0003-0526-5473; Email: huangfq@sjtu.edu.cn

Hui Bi − *Key laboratory of Intelligent Creation for Extreme Energy Materials of the Ministry of Education, School of Materials Science and Engineering, and Zhang Jiang Institute for Advanced Study, Shanghai Jiao Tong University, Shanghai 200240, China*; Email: bihui@sjtu.edu.cn

Wei Zhao − *State Key Laboratory of High Performance Ceramics and Superfine Microstructures, Shanghai Institute of Ceramics, Chinese Academy of Sciences, Shanghai 200050, China*; Email: zhaowei220@mail.sic.ac.cn

Authors

Meijing Xiao − *State Key Laboratory of High Performance Ceramics and Superfine Microstructures, Shanghai Institute of Ceramics, Chinese Academy of Sciences, Shanghai 200050, China; Key laboratory of Intelligent Creation for Extreme Energy Materials of the Ministry of Education, School of Materials Science and Engineering, and Zhang Jiang Institute for Advanced Study, Shanghai Jiao Tong University, Shanghai 200240, China; Center of Materials Science and Optoelectronics Engineering, University of Chinese Academy of Sciences, Beijing 100049, China*

Ce Zhou − *Beijing Nadi Technology Co., Ltd., Beijing 102628, China*

Yuge Cao − *State Key Laboratory of High Performance Ceramics and Superfine Microstructures, Shanghai Institute of Ceramics, Chinese Academy of Sciences, Shanghai 200050, China; Key laboratory of Intelligent Creation for Extreme Energy Materials of the Ministry of Education, School of Materials Science and Engineering, and Zhang Jiang Institute for Advanced Study, Shanghai Jiao Tong University, Shanghai 200240, China*

Tianxun Cai − *State Key Laboratory of High Performance Ceramics and Superfine Microstructures, Shanghai Institute of Ceramics, Chinese Academy of Sciences, Shanghai 200050, China*

Shiyu Zhang − *State Key Laboratory of High Performance Ceramics and Superfine Microstructures, Shanghai Institute of Ceramics, Chinese Academy of Sciences, Shanghai 200050, China; Key laboratory of Intelligent Creation for Extreme Energy Materials of the Ministry of Education, School of Materials Science and Engineering, and Zhang Jiang Institute for Advanced Study, Shanghai Jiao Tong University, Shanghai 200240, China*

ZhengYao Li − *Neutron Scattering Laboratory, China Institute of Atomic Energy, Beijing 102413, China;* orcid.org/0000-0002-0149-5864

Kai Sun − *Neutron Scattering Laboratory, China Institute of Atomic Energy, Beijing 102413, China*

Dongfeng Chen − *Neutron Scattering Laboratory, China Institute of Atomic Energy, Beijing 102413, China*

Hongliang Dong − *Center for High Pressure Science and Technology Advanced Research, Shanghai 201203, China; Shanghai Key Laboratory of Material Frontiers Research in Extreme Environments (MFree), Institute for Shanghai Advanced Research in Physical Sciences (SHARPS), Shanghai 201203, China*

Complete contact information is available at: https://pubs.acs.org/10.1021/jacs.5c23314

Author Contributions

◆M.X., C.Z., and W.D. contributed equally to this work. The manuscript was written through the contributions of all authors. All authors have given approval to the final version of the manuscript.

Funding

National Key R&D Program of China (2025YFF0516300), National Natural Science Foundation of China (22471283 and 22561160126), Science and Technology Commission of Shanghai Municipality (23DZ1200800), the Youth Innovation Promotion Association CAS (2021246).

Notes

The authors declare no competing financial interest.

■ ACKNOWLEDGMENTS

This work is supported by the National Natural Science Foundation of China (22471283 and 22561160126), Science and Technology Commission of Shanghai Municipality (23DZ1200800), National Key R&D Program of China (2025YFF0516300), and the Youth Innovation Promotion Association CAS (2021246), and Science and Technology Cooperation Program of Shanghai Jiao Tong in Inner Mongolia Autonomous Region—Action Plan of Shanghai Jiao Tong University for "Revitalizing Inner Mongolia through Science and Technology". The authors would like to thank Dr. Qing Wang for her cooperation and help. The authors would also like to thank the Shanghai Synchrotron Radiation Facility of BL14W1 (https://cstr.cn/31124.02.SSRF.BL14W1) and BL14B1 (https://cstr.cn/31124.02.SSRF.BL14B1) for the assistance with XAFS and SXRD measurements, and the China Advanced Research Reactor (CARR) for the support with NPD measurements.

REFERENCES

(1) Zhao, C. L.; Wang, Q. D.; Yao, Z. P.; Wang, J. L.; Sanchez-Lengeling, B.; Ding, F. X.; Qi, X. G.; Lu, Y. X.; Bai, X. D.; Li, B. H.; Li, H.; Aspuru-Guzik, A.; Huang, X. J.; Delmas, C.; Wagemaker, M.; Chen, L. Q.; Hu, Y. S. Rational design of layered oxide materials for sodium-ion batteries. *Science* **2020**, *370* (6517), 708−711.

(2) Xiong, P. X.; Bai, P. X.; Li, A.; Li, B. F.; Cheng, M. R.; Chen, Y. P.; Huang, S. P.; Iang, Q.; Bu, X. H.; Xu, Y. H. Bismuth Nanoparticle@Carbon Composite Anodes for Ultralong Cycle Life and High-Rate Sodium-Ion Batteries. *Adv. Mater.* **2019**, *31* (48), No. 1904771.

(3) Li, K. K.; Zhang, J.; Lin, D. M.; Wang, D. W.; Li, B. H.; Lv, W.; Sun, S.; He, Y. B.; Kang, F. Y.; Yang, Q. H.; Zhou, L. M.; Zhang, T. Y. Evolution of the electrochemical interface in sodium ion batteries with ether electrolytes. *Nat. Commun.* **2019**, *10*, No. 725.

(4) Huang, H. J.; Xu, R.; Feng, Y. Z.; Zeng, S. F.; Jiang, Y.; Wang, H. J.; Luo, W.; Yu, Y. Sodium/Potassium-Ion Batteries: Boosting the Rate Capability and Cycle Life by Combining Morphology, Defect and Structure Engineering. *Adv. Mater.* **2020**, *32* (8), No. 1904320.

(5) Cao, Y. G.; Xiao, M. J.; Sun, X. Z.; Dong, W. J.; Huang, F. Q. Recent Advances on High-Capacity Sodium Manganese-Based Oxide Cathodes for Sodium-ion Batteries. *Chem. - Eur. J.* **2022**, *29*, No. e202202997.

(6) Dong, W. J.; Le, J. B.; Jin, Y.; Zhang, G. Q.; Ye, B.; Qin, P.; Huang, F. Q. Metal organophosphates: electronic structure tuning from inert materials to universal alkali-metal-ion battery cathodes. *Rare Met.* **2023**, *42* (1), 122−133.

(7) Mu, J. X.; Cai, T. X.; Dong, W. J.; Zhou, C.; Han, Z.; Huang, F. Q. Biphasic high-entropy layered oxide as a stable and high-rate cathode for sodium-ion batteries. *Chem. Eng. J.* **2023**, *471*, No. 144403.

(8) de la Llave, E.; Talaie, E.; Levi, E.; Nayak, P. K.; Dixit, M.; Rao, P. T.; Hartmann, P.; Chesneau, H. F.; Major, D. T.; Greenstein, M.; Aurbach, D.; Nazar, L. F. Improving Energy Density and Structural Stability of Manganese Oxide Cathodes for Na-Ion Batteries by Structural Lithium Substitution. *Chem. Mater.* **2016**, *28* (24), 9064−9076.

(9) Yang, L. F.; Li, X.; Liu, J.; Xiong, S.; Ma, X. T.; Liu, P.; Bai, J. M.; Xu, W. Q.; Tang, Y. Z.; Hu, Y. Y.; Liu, M. L.; Chen, H. Lithium-Doping Stabilized High-Performance P2-Na0.66Li0.18Fe0.12Mn0.7O2 Cathode for Sodium Ion Batteries. *J. Am. Chem. Soc.* **2019**, *141* (16), 6680−6689.

(10) Hwang, J. Y.; Kim, J.; Yu, T. Y.; Sun, Y. K. A New P2-Type Layered Oxide Cathode with Extremely High Energy Density for Sodium-Ion Batteries. *Adv. Energy Mater.* **2019**, *9* (15), No. 1803346.

(11) Su, C.; Liu, G.; Sun, Q.; Wen, L.; Chen, Z.; Zhao, M. New Strategy to Build a High-Performance P′2-Type Cathode Material through Oxygen Vacancies and Mg Substitution for Sodium-Ion Batteries. *ACS Appl. Energy Mater.* **2024**, *7* (5), 1927−1937.

(12) Chen, X.; Lin, G.; Liu, P.; Sun, Z.; Si, Y.; Wang, Q.; Jiao, L. Synergetic enhancement of structural stability and kinetics of P′2-type layered cathode for sodium-ion batteries via cation−anion co-doping. *Energy Storage Mater.* **2024**, *67*, No. 103303, DOI: 10.1016/j.ensm.2024.103303.

(13) Ji, H.; Ren, H.; Chen, G.; Ji, W.; Zhou, F.; Qu, H.; Fang, H.; Chu, M.; Qi, R.; Zhai, J.; Zeng, W.; Liu, T.; Zhou, G.; Xiao, Y.; Lu, J. Structural Insights Into Phase Formation of Sodium Layered Cathodes Materials with Prominent Electrochemical Performances. *Angew. Chem., Int. Ed.* **2025**, *64* (37), No. e202510981, DOI: 10.1002/anie.202510981.

(14) Gui, X.; Xiang, Z.; Ren, T.; Liu, W.; Pei, Z.; Long, G.; Fu, Z.; Wan, K.; Liang, Z. High-Entropy Doped P′2 Mn-Based Layered Oxide with Superior Stability and High Capacity for Sodium-Ion Batteries. *Adv. Mater.* **2025**, *37* (20), No. 2417008, DOI: 10.1002/adma.202417008.

(15) Li, C.; Li, M.; Liu, G.; Zhuo, H.; Li, Q.; Zhang, H.; Pang, G.; Yang, X.; Liao, Z.; Wang, K.; Wang, D.; Xiao, B.; Geng, D. Achieving Superior Cyclability Pouch Cells with Oxygen Vacancy-Moderated P′2/P3 Hybrid Layered Sodium Cathode Materials. *ACS Appl. Mater. Interfaces* **2024**, *16* (35), 46216−46225.

(16) Kumakura, S.; Tahara, Y.; Kubota, K.; Chihara, K.; Komaba, S. Sodium and Manganese Stoichiometry of P2-Type Na2/3MnO2. *Angew. Chem., Int. Ed.* **2016**, *55* (41), 12760−12763.

(17) Fang, H.; Ji, H.; Zhai, J.; Wang, C.; Zhu, C.; Chen, G.; Chu, M.; Zhang, T.; Ma, Z.; Zhao, W.; Ji, W.; Xiao, Y. Mitigating Jahn−Teller Effect in Layered Cathode Material Via Interstitial Doping for High-Performance Sodium-Ion Batteries. *Small* **2023**, *19* (35), No. 2301360, DOI: 10.1002/smll.202301360.

(18) Peng, B.; Sun, Z.; Jiao, S.; Wang, G.; Zhang, G. Electrochemical Performance Optimization of Layered P2-Type Na0.67MnO2 through Simultaneous Mn-Site Doping and Nanostructure Engineering. *Batteries Supercaps* **2020**, *3* (2), 147−154.

(19) Jin, J.; Liu, Y.; Shen, Q.; Zhao, X.; Zhang, J.; Song, Y.; Li, T.; Xing, X.; Chen, J. Unveiling the Complementary Manganese and Oxygen Redox Chemistry for Stabilizing the Sodium-Ion Storage Behaviors of Layered Oxide Cathodes. *Adv. Funct. Mater.* **2022**, *32* (29), No. 2203424, DOI: 10.1002/adfm.202203424.

(20) Wang, P.-F.; Xiao, Y.; Piao, N.; Wang, Q.-C.; Ji, X.; Jin, T.; Guo, Y.-J.; Liu, S.; Deng, T.; Cui, C.; Chen, L.; Guo, Y.-G.; Yang, X.-Q.; Wang, C. Both cationic and anionic redox chemistry in a P2-type sodium layered oxide. *Nano Energy* **2020**, *69*, No. 104474, DOI: 10.1016/j.nanoen.2020.104474.

(21) Wang, Y.; Zhao, X.; Jin, J.; Shen, Q.; Zhang, N.; Qu, X.; Liu, Y.; Jiao, L. Low-cost layered oxide cathode involving cationic and anionic redox with a complete solid-solution sodium-storage behavior. *Energy Storage Mater.* **2022**, *47*, 44−50.

(22) Liu, S.; Wan, J.; Ou, M.; Zhang, W.; Chang, M.; Cheng, F.; Xu, Y.; Sun, S.; Luo, C.; Yang, K.; Fang, C.; Han, J. Regulating Na Occupation in P2-Type Layered Oxide Cathode for All-Climate Sodium-Ion Batteries. *Adv. Energy Mater.* **2023**, *13* (11), No. 2203521, DOI: 10.1002/aenm.202203521.

(23) Gao, M.; Li, H.; Zhao, Z.; Wang, X. Inducing Na+ Site Rearrangement Through a Cosubstitution Strategy for Rapid Na Diffusion Kinetics of P2-Type Layered Metal Oxides. *ACS Appl. Mater. Interfaces* **2024**, *16* (12), 14789−14798.

(24) Sun, Y.; Zhou, P.; Liu, S.; Zhao, Z.; Pan, Y.; Shen, X.; Wu, X.; Zhao, J.; Weng, J.; Zhou, J. Manipulating Na occupation and constructing protective film of P2-Na0.67Ni0.33Mn0.67O2 as long-term cycle stability cathode for sodium-ion batteries. *J. Energy Chem.* **2024**, *88*, 603−611.

(25) Su, C.; Liu, G. Q.; Liu, G. Y.; Wen, L. A new synthesis route of high-performance P ′ 2-Na0.67Fe0.1Mn0.9O2-x and its sodium storage properties for sodium-ion batteries. *J. Power Sources* **2023**, *576*, No. 233228.

(26) Kim, E. J.; Hosaka, T.; Kubota, K.; Tatara, R.; Kumakura, S.; Komaba, S. Effect of Cu Substitution in P′2- and P2-Type Sodium Manganese-Based Oxides. *ACS Appl. Energy Mater.* **2022**, *5* (10), 12999−13010.

(27) Wang, Q. C.; Shadike, Z.; Li, X. L.; Bao, J.; Qiu, Q. Q.; Hu, E.; Bak, S. M.; Xiao, X.; Ma, L.; Wu, X. J.; Yang, X. Q.; Zhou, Y. N. Tuning Sodium Occupancy Sites in P2-Layered Cathode Material for Enhancing Electrochemical Performance. *Adv. Energy Mater.* **2021**, *11* (13), No. 2003455, DOI: 10.1002/aenm.202003455.

(28) Shi, Q.; Qi, R.; Feng, X.; Wang, J.; Li, Y.; Yao, Z.; Wang, X.; Li, Q.; Lu, X.; Zhang, J.; Zhao, Y. Niobium-doped layered cathode material for high-power and low-temperature sodium-ion batteries. *Nat. Commun.* **2022**, *13* (1), No. 3205, DOI: 10.1038/s41467-022-30942-z.

(29) <Studies of the layered manganese bronzes, Na2−3[Mn1−xMx]O2 with M = Co, Ni, Li, and Li2−3[Mn1−xMx]O2 prepared by ion-exchange.pdf>.

(30) Liu, X. S.; Yuan, C.; Zheng, X. Y.; Cheng, G. Y.; Qian, H.; Zheng, B. Z.; Lu, X. Y.; Yang, Y.; Zhu, Y. Z.; Xiang, Y. X. Stabilizing Interlayer Repulsion in Layered Sodium-Ion Oxide Cathodes via Hierarchical Layer Modification. *Adv. Mater.* **2024**, *36* (38), No. 2407519, DOI: 10.1002/adma.202407519.

(31) Liu, X.; Zhong, G.; Xiao, Z.; Zheng, B.; Zuo, W.; Zhou, K.; Liu, H.; Liang, Z.; Xiang, Y.; Chen, Z.; Ortiz, G. F.; Fu, R.; Yang, Y. Al and Fe-containing Mn-based layered cathode with controlled vacancies for high-rate sodium ion batteries. *Nano Energy* **2020**, *76*, No. 104997, DOI: 10.1016/j.nanoen.2020.104997.
(32) Zhao, C.; Li, C.; Liu, H.; Qiu, Q.; Geng, F.; Shen, M.; Tong, W.; Li, J.; Hu, B. Coexistence of (O2)n− and Trapped Molecular O2 as the Oxidized Species in P2-Type Sodium 3d Layered Oxide and Stable Interface Enabled by Highly Fluorinated Electrolyte. *J. Am. Chem. Soc.* **2021**, *143* (44), 18652−18664.
(33) Clément, R. J.; Xu, J.; Middlemiss, D. S.; Alvarado, J.; Ma, C.; Meng, Y. S.; Grey, C. P. Direct evidence for high Na+mobility and high voltage structural processes in P2-Nax[LiyNizMn1−y−z]O2(x, y, $z \leq 1$) cathodes from solid-state NMR and DFT calculations. *J. Mater. Chem. A* **2017**, *5* (8), 4129−4143.
(34) Su, G. Q.; Li, L. J.; Shi, Z.; Ma, X. B.; Ma, L.; Cao, Z. J. Boosting anionic redox through lithium doping in P2-layered cathode for high-performance sodium-ion batteries. *Appl. Surf. Sci.* **2023**, *608*, No. 155097.
(35) Su, Z.; Li, S.; Ma, L.; Liu, T.; Li, M.; Wu, T.; Zhang, Q.; Dong, C.; Lai, C.; Gu, L.; Lu, J.; Pan, F.; Zhang, S. Quenching-Induced Defects Liberate the Latent Reversible Capacity of Lithium Titanate Anode. *Adv. Mater.* **2022**, *35* (5), No. 2208573, DOI: 10.1002/adma.202208573.
(36) Jin, J. T.; Liu, Y. C.; Zhao, X. D.; Liu, H.; Deng, S. Q.; Shen, Q. Y.; Hou, Y.; Qi, H.; Xing, X. R.; Jiao, L. F.; Chen, J. Annealing in Argon Universally Upgrades the Na-Storage Performance of Mn-Based Layered Oxide Cathodes by Creating Bulk Oxygen Vacancies. *Angew. Chem., Int. Ed.* **2023**, *62*, No. e202219230, DOI: 10.1002/anie.202219230.
(37) Chen, Z. W.; Yang, M. L.; Chen, G. J.; Tang, G. X.; Huang, Z. Y.; Chu, M. H.; Qi, R.; Li, S. M.; Wang, R.; Wang, C. Q.; Zhang, T. L.; Zhai, J. J.; Zhao, W. G.; Zhang, J. R.; Chen, J.; He, L. H.; Xu, J. P.; Yin, W.; Wang, J.; Xiao, Y. G. Triggering anionic redox activity in Fe/Mn-based layered oxide for high-performance sodium-ion batteries. *Nano Energy* **2022**, *94*, No. 106958.
(38) Li, L. J.; Su, G. Q.; Lu, C.; Ma, X. B.; Ma, L.; Wang, H. L.; Cao, Z. J. Effect of lithium doping in P2-Type layered oxide cathodes on the electrochemical performances of Sodium-Ion batteries. *Chem. Eng. J.* **2022**, *446*, No. 136923.
(39) Li, C. F.; Li, A.; Li, M. J.; Xiong, P. X.; Liu, Y. S.; Cheng, M. R.; Geng, D. L.; Xu, Y. H. Ultrafast Synthesis of Layered Transition-Metal Oxide Cathodes from Metal-Organic Frameworks for High-Capacity Sodium-Ion Batteries. *ACS Appl. Mater. Interfaces* **2022**, *14* (21), 24462−24468.
(40) Tan, L.; Wu, Q. F.; Liu, Z. S.; Chen, Q. H.; Yi, H. L.; Zhao, Z. X.; Song, L. B.; Zhong, S. K.; Wu, X. W.; Li, L. J. Ti-substituted O3-type layered oxide cathode material with high-voltage stability for sodium-ion batteries. *J. Colloid Interface Sci.* **2022**, *622*, 1037−1044.
(41) Wang, K.; Wu, Z.-G.; Melinte, G.; Yang, Z.-G.; Sarkar, A.; Hua, W.; Mu, X.; Yin, Z.-W.; Li, J.-T.; Guo, X.-D.; Zhong, B.-H.; Kübel, C. Preparation of intergrown P/O-type biphasic layered oxides as high-performance cathodes for sodium ion batteries. *J. Mater. Chem. A* **2021**, *9* (22), 13151−13160.
(42) Xue, Z.-C.; Huang, J.-n.; Guo, X.; Guo, H.; Zhu, Y.; Hu, G.-r.; Peng, Z.-d.; Cao, Y.-b.; Du, K. Capturing surface interlayer cation migration in Na0.6[Li0.2Mn0.8]O2 layered cathode materials for sodium battery. *Ceram. Int.* **2022**, *48* (17), 25642−25646.
(43) Huang, J.; Sun, L.; Pan, X.; Hong, N.; Hu, X.; Li, D.; Wang, H.; Shu, Y.; Zeng, J.; Jian, W.; He, Y.; Deng, W.; Zou, G.; Hou, H.; Ji, X. Native Defect Elimination and Lattice Framework Reinforcement Toward Ultra-Stable Sodium-Ion Layered Cathodes. *Adv. Mater.* **2025**, *37* (34), No. 2506273, DOI: 10.1002/adma.202506273.
(44) Sun, L.; Wu, Z.; Hou, M.; Ni, Y.; Sun, H.; Jiao, P.; Li, H.; Zhang, W.; Zhang, L.; Zhang, K.; Cheng, F.; Chen, J. Unraveling and suppressing the voltage decay of high-capacity cathode materials for sodium-ion batteries. *Energy Environ. Sci.* **2024**, *17* (1), 210−218.
(45) Wang, Y.; Sun, Z.; Jin, J.; Zhao, X.; Qu, X.; Jiao, L.; Liu, Y. In Situ Bulk Oxygen Vacancy Manufacturing and Surface Spinel Layer Coating Enable High-Performance Na-Ion Layered Fe−Mn Based Cathodes. *Adv. Funct. Mater.* **2025**, *35* (38), No. 2504354, DOI: 10.1002/adfm.202504354.
(46) Xiao, B. W.; Wang, Y. C.; Tan, S.; Song, M.; Li, X.; Zhang, Y. X.; Lin, F.; Han, K. S.; Omenya, F.; Amine, K.; Yang, X. Q.; Reed, D.; Hu, Y. Y.; Xu, G. L.; Hu, E. Y.; Li, X.; Li, X. L. Vacancy-Enabled O3 Phase Stabilization for Manganese-Rich Layered Sodium Cathodes. *Angew. Chem., Int. Ed.* **2021**, *60* (15), 8258−8267.
(47) Boivin, E.; House, R. A.; Marie, J. J.; Bruce, P. G. Controlling Iron Versus Oxygen Redox in the Layered Cathode Na0.67Fe0.5Mn0.5O2: Mitigating Voltage and Capacity Fade by Mg Substitution. *Adv. Energy Mater.* **2022**, *12* (30), No. 2200702, DOI: 10.1002/aenm.202200702.
(48) Yan, P. F.; Zheng, J. M.; Tang, Z. K.; Devaraj, A.; Chen, G. Y.; Amine, K.; Zhang, J. G.; Liu, L. M.; Wang, C. M. Injection of oxygen vacancies in the bulk lattice of layered cathodes. *Nat. Nanotechnol.* **2019**, *14* (6), 602−608.
(49) Kumakura, S.; Tahara, Y.; Sato, S.; Kubota, K.; Komaba, S. P′2-Na2/3Mn0.9Me0.1O2 (Me = Mg, Ti, Co, Ni, Cu, and Zn): Correlation between Orthorhombic Distortion and Electrochemical Property. *Chem. Mater.* **2017**, *29* (21), 8958−8962.
(50) Jin, T.; Wang, P. F.; Wang, Q. C.; Zhu, K. J.; Deng, T.; Zhang, J. X.; Zhang, W.; Yang, X. Q.; Jiao, L. F.; Wang, C. S. Realizing Complete Solid-Solution Reaction in High Sodium Content P2-Type Cathode for High-Performance Sodium-Ion Batteries. *Angew. Chem., Int. Ed.* **2020**, *59* (34), 14511−14516.
(51) Singh, G.; Tapia-Ruiz, N.; del Amo, J. M. L.; Maitra, U.; Somerville, J. W.; Armstrong, A. R.; de Ilarduya, J. M.; Rojo, T.; Bruce, P. G. High Voltage Mg-Doped Na0.67Ni0.3-xMgxMn0.7O2 (x = 0.05, 0.1) Na-Ion Cathodes with Enhanced Stability and Rate Capability. *Chem. Mater.* **2016**, *28* (14), 5087−5094.
(52) Yang, L.; Liu, Z. P.; Shen, X.; Li, S. W.; Hu, Z. W.; Kong, Q. Y.; Ma, J.; Li, J. D.; Lin, H. J.; Chen, C. T.; Chen, J. M.; Haw, S. C.; Wang, X. F.; Yu, R. C.; Wang, Z. X.; Chen, L. Q. Effect of vacancy-tailored Mn3+ spinning on enhancing structural stability. *Energy Storage Mater.* **2022**, *44*, 231−238.
(53) Ye, F.; Liao, H.; Shen, Y.; Luo, J.; Du, J.; Xia, Z.; Ai, Y.; Yang, S.; Wang, Y.; Zhang, X.; Chen, J.; Huang, F. Manganese Segregation in Layered Oxide Cathode by Deep Eutectic Solvent Synthesis toward High-Voltage Sodium Storage. *ACS Nano* **2025**, *19* (46), 40023−40033.
(54) Xu, J.; Sun, M.; Qiao, R.; Renfrew, S. E.; Ma, L.; Wu, T.; Hwang, S.; Nordlund, D.; Su, D.; Amine, K.; Lu, J.; McCloskey, B. D.; Yang, W.; Tong, W. Elucidating anionic oxygen activity in lithium-rich layered oxides. *Nat. Commun.* **2018**, *9* (1), No. 947, DOI: 10.1038/s41467-018-03403-9.
(55) Deng, Y. Y.; Jin, T.; Li, C.; Zhang, T.; Zhang, W. J.; Cui, S. J.; Shen, C.; Jiao, L. F.; Huang, H. T.; Xie, K. Y. Lattice strengthening enables reversible anionic redox chemistry in sodium-ion batteries. *Energy Storage Mater.* **2025**, *74*, No. 103935, DOI: 10.1016/j.ensm.2024.103935.
(56) Dong, W. J.; Xie, M.; Zhao, S. W.; Qin, Q. L.; Huang, F. Q. Materials design and preparation for high energy density and high power density electrochemical supercapacitors. *Mater. Sci. Eng., R* **2023**, *152*, No. 100713.
(57) Shakouri, S.; Abouzari-Lotf, E.; Chen, J.; Diemant, T.; Klyatskaya, S.; Pammer, F. D.; Mizuno, A.; Fichtner, M.; Ruben, M. Molecular Engineering of Metalloporphyrins for High-Performance Energy Storage: Central Metal Matters. *ChemSusChem* **2023**, *16*, No. e202202090, DOI: 10.1002/cssc.202202090.